

LASER INTERFEROMETER GRAVITATIONAL WAVE OBSERVATORY
- LIGO -
CALIFORNIA INSTITUTE OF TECHNOLOGY
MASSACHUSETTS INSTITUTE OF TECHNOLOGY

Publication	LIGO-P990004-A - D	7/8/99
Spatiotemporal Model of the LIGO Interferometer		
R. G. Beausoleil and D. Sigg		

Distribution of this draft:

all

This is an internal working note
of the LIGO Project.

LIGO Hanford Observatory
P.O. Box 1970 S9-02
Richland, WA 99352
Phone (509) 372-8106
FAX (509) 372-8137
E-mail: info@ligo.caltech.edu

LIGO Livingston Observatory
19100 LIGO Lane
Livingston, LA 70754
Phone (504) 686-3100
FAX (504) 686-7189
E-mail: info@ligo.caltech.edu

California Institute of Technology
LIGO Project - MS 51-33
Pasadena CA 91125
Phone (626) 395-2129
Fax (626) 304-9834
E-mail: info@ligo.caltech.edu

Massachusetts Institute of Technology
LIGO Project - MS NW17-161
Cambridge, MA 01239
Phone (617) 253-4824
Fax (617) 253-7014
E-mail: info@ligo.mit.edu

WWW: <http://www.ligo.caltech.edu/>

Spatiotemporal Model of the LIGO Interferometer

R. G. Beausoleil*

Edward L. Ginzton Laboratory, Stanford University, Stanford, CA 94305

D. Sigg

LIGO Hanford Observatory, P.O. Box 1970 S9-02, Richland, WA 99352

We develop a detailed spatiotemporal model in the adiabatic approximation of the optical response of the Laser Interferometer Gravitational-Wave Observatory (LIGO) optical system to environmental perturbations. We begin by deriving a first-order linear time-dependent evolution equation that models the electromagnetic field as a function of position within a Fabry-Perot interferometer. This model allows both the length of the resonator and the misalignment angles of the end mirrors to vary in time, and describes both resonant and nonresonant phenomena. After defining a biorthogonality relation that must be satisfied by general unperturbed spatial eigenfunctions of the Fabry-Perot interferometer, we expand the intracavity field as a linear combination of these functions, and convert the spatiotemporal evolution equation into a linear system of coupled time-dependent iteration and/or differential equations. We then calculate the adiabatic connection equations that link the two LIGO Fabry-Perot interferometers through the power recycling cavity, which is comprised of two mirrors (the power recycling input mirror and the beamsplitter) that have the same mechanical degrees of freedom as those in the Fabry-Perot arm cavities. We develop a detailed instance of this model for the evolution of the intracavity field within a resonator with sufficiently small misalignment angles that a Hermite-Gauss basis set can be used. We develop a detailed general approach to signal demodulation for simulation of servo-control systems, and describe its implementation in the Hermite-Gauss approximation for cartesian split-plane detectors. Finally, we demonstrate the use of this small-angle model to simulate the effect of angular misalignment on the longitudinal response function.

I. INTRODUCTION

Currently, a new generation of long-baseline laser interferometer gravitational wave detectors is under construction [1–4]. Their design sensitivity is of order $\Delta L/L \approx 10^{-21}$ r.m.s., integrated over a 100 Hz bandwidth centered at the minimum noise region. The Laser Interferometer Gravitational-wave Observatory (LIGO) will implement a power-recycled Michelson interferometer with Fabry-Perot arm cavities. This design was chosen to optimize the shot noise limited sensitivity in the gravitational wave band in the neighborhood of 100 Hz to 200 Hz by maximizing the light power in the arms, but without storing the light in the Fabry-Perot arm cavities significantly longer than the period of the gravitational waves.

Among the most significant obstacles to the development of an efficient time-domain description of the LIGO optical configuration are the vastly different time scales involved. For example, the smallest time scale is given by the round-trip time in the power recycling cavity, which is about 63 ns, while the total light storage time—which determines the relaxation time of the system—is about 1 s. Two other important time scales are the round-trip time of an arm cavity which is about 30 μ s, and their storage time which is about 10 ms. Also, because of the highly non-linear temporal character of a coupled cavity-system, the dynamical behaviour can be non-trivial. As a result, most of the past LIGO modeling work has been restricted to (i) analytic approaches treating small effects as deviations from exact resonance [5,6], (ii) static descriptions of spatial uniformities—based on either FFT methods [7–9] or Hermite-Gauss cavity eigenmode expansions [10–12], and (iii) dynamic simulations with *no* spatial representation [13].

An improved model of the LIGO interferometer would describe concurrently the effects of both spatial and temporal environmental perturbations on the intracavity electromagnetic fields. In the general case, this problem is complicated by statically-characterized diffractive losses at the apertures presented by intracavity optics (such as mirrors and beamsplitters) which become important throughout the coupled-cavity system when one or more of the mirrors are misaligned significantly. In practice, the presence of these apertures means that round-trip spatial propagators are *not* Hermitian. [14,15] Eigenmodes of non-Hermitian systems are not orthogonal in general, but satisfy a biorthogonality relationship that allows us to compute matrix elements of those propagators. Therefore, we seek an expansion of the intracavity field in some arbitrary spatial eigenmode set; since the Hermite-Gauss eigenmodes are both orthogonal and biorthogonal, our formalism supports both the small-angle Hermite-Gauss approximation and more accurate large-angle representations, and we can move from one representation to another simply by recomputing the propagator matrix elements. All other features of the model (e.g., coupling dynamics, detection schemes) are invariant under this change of spatial basis.

In the following sections, we derive the equations and approximations necessary to efficiently model the spatiotemporal response of the LIGO interferometer to environmental perturbations. Section II treats the important case of a single Fabry-Perot cavity, since we will choose the round-trip time of either Fabry-Perot arm cavity as the characteristic time scale of the model. We develop a set of time-dependent evolution equations that simulate the reponse of the Fabry-Perot intracavity field to changes in the positions and alignment angles of the mirrors, and to changes in the amplitudes of the incident input field. Depending on the resonance condition of the field under test, the evolution equation is either iterative or differential, and is efficient enough to allow practical simulations over time intervals as long as 1 s. Section III extends this formalism to the LIGO configuration, using the adiabatic approximation (justified by the 63 ns round-trip time in the power recycling cavity) to generate a set of steady-state matrix coupling equations. After developing a representation of demodulation detectors for servo-control systems, section IV presents the results of a simulation of the effect of angular misalignment on the longitudinal response function of the interferometer.

II. ELECTROMAGNETIC FIELD EVOLUTION EQUATIONS FOR A FABRY-PEROT INTERFEROMETER

A. Paraxial Electromagnetic Field Propagation

Consider the generalized Fabry-Perot resonator shown schematically in Fig. 1, with an unperturbed length $L_0 \equiv N\lambda_0/2$, where N is a (very large) integer and $\lambda_0 \equiv 2\pi/k_0 \equiv 2\pi c/\omega_0$ is the wavelength of the incident laser electric field $\mathbf{F}(\mathbf{r}, t)$ with angular carrier frequency ω_0 . This incident field is transmitted through the inbound test mass (ITM) \mathcal{M}_1 and propagates in the positive z direction. We represent this incident field as the real part of a product of a real time-independent polarization unit vector \mathbf{e} , a complex amplitude function $F(\mathbf{r}, t)$, and the carrier wave function $\exp[i(k_0z - \omega_0t)]$:

$$\mathbf{F}(\mathbf{r}, t) \equiv \text{Re} \{ \mathbf{e} F(\mathbf{r}, t) \exp[i(k_0z - \omega_0t)] \}. \quad (1)$$

We use the amplitude function $F(\mathbf{r}, t)$ to represent any closely-spaced frequency components (such as radio-frequency-modulated sidebands) as

$$F(\mathbf{r}, t) \equiv \sum_q F_q(\mathbf{r}, t) \exp[i(k_qz - \omega_qt)], \quad (2)$$

where the summation is taken over all frequency components (including the carrier), $F_q(\mathbf{r}, t)$ is the complex amplitude function of component q , and $\Delta\omega_q = \Delta k_q/c \ll \omega_0$ is the angular frequency shift of component q . By convention, the carrier is labeled by $q = 0$, and therefore $\Delta\omega_0 = 0$. We express all field amplitudes in units of $\sqrt{W/\text{cm}^2}$, so that the time-averaged intensity carried by $\mathbf{F}(\mathbf{r}, t)$ is $I(\mathbf{r}, t) = \frac{1}{2} \sum_q |F_q(\mathbf{r}, t)|^2$.

For the purpose of developing a time-dependent model that describes the evolution of the intracavity field under the influence of environmental perturbations, we define a forward-propagating field that circulates within the cavity in the positive z direction (i.e., in the same sense as the incident electric field relative to the defined reference plane at $z = 0$). We assume that the cavity contains no nonlinear optical or polarization rotation elements. Hence, the intracavity field has the same polarization \mathbf{e} as the transmitted field $\mathbf{F}(\mathbf{r}, t)$, and may be represented using the same discrete frequency decomposition as in Eq. (1):

$$\mathbf{E}(\mathbf{r}, t) \equiv \text{Re} \{ \mathbf{e} E(\mathbf{r}, t) \exp[i(k_0z - \omega_0t)] \}, \quad (3)$$

where (as above) $E(\mathbf{r}, t) \equiv \sum_q E_q(\mathbf{r}, t) \exp[i(k_qz - \omega_qt)]$.

In the case of an open-sided standing-wave optical resonator with finite-aperture mirrors, at any time t and intracavity reference plane z the transverse spatial dependence of $E(\mathbf{r}, t)$ satisfies the paraxial Helmholtz equation [15]

$$\nabla_{\perp}^2 E(\mathbf{r}, t) - i 2 k_0 \partial_z E(\mathbf{r}, t) = 0, \quad (4)$$

where $\nabla_{\perp}^2 \equiv \partial_x^2 + \partial_y^2$. Hence, if the transverse field is known at one reference plane z_1 containing an aperture \mathcal{A}_1 , then we can employ Huygens's integral in the Fresnel approximation to obtain the field at a new reference plane z_2 after propagating through a paraxial optical system described by the corresponding $ABCD$ ray transfer matrix. [16] Temporarily suppressing the common fixed time label t , the Huygens-Fresnel integral has the form [14]

$$E(x, y, z_2) = \int_{\mathcal{A}_1} dx' dy' \rho_1(x', y') K_{21}(x, y; x', y') E(x', y', z_1) \equiv \hat{K}_{21}[E(x', y', z_1)], \quad (5)$$

where the functional form of the forward propagation kernel for a cylindrically symmetric paraxial system is

$$K_{21}(x, y; x', y') = \frac{1}{i\lambda B} \exp \left\{ i \frac{\pi}{\lambda B} [A(x'^2 + y'^2) - 2(x'x + y'y) + D(x^2 + y^2)] \right\}. \quad (6)$$

The presence of the complex reflection coefficient $\rho_1(x, y)$ of aperture \mathcal{A}_1 ensures that $E(\mathbf{r})$ automatically satisfies the boundary condition

$$E(x, y, z_1^+) = \rho_1(x, y) E(x, y, z_1^-) \quad (7)$$

at reference plane z_1 , where z_1^- is located at the reference plane prior to reflection from \mathcal{M}_1 , and z_1^+ labels the field position just after reflection has occurred.

We can apply this approach to the propagation of the field around one complete circuit through the resonator using two successive steps from each mirror to the next, as shown in Fig. 1 and the equivalent round-trip lens guide shown in Fig. 2. We describe the paraxial optical system between the two mirrors with a general $ABCD$ matrix (although in practice the LIGO paraxial matrix elements have the values $A_1 = D_1 = 1$, $B_1 = L_0 \cong 4$ km, and $C_1 = 0$), and we initially ignore any anomalous phase distortions caused by misalignment. The first propagation step carries the field from the aperture \mathcal{A}_1 at the reference plane $z_1 = 0$ (located just *before* the reflection from the ITM), through both the reflection from the ITM and the intracavity paraxial system, to the reference plane $z_2 = L_0$ at the aperture \mathcal{A}_2 . For this step, the $ABCD$ matrix elements are given by

$$\begin{bmatrix} A & B \\ C & D \end{bmatrix} = \begin{bmatrix} A_1 & B_1 \\ C_1 & D_1 \end{bmatrix} \cdot \begin{bmatrix} 1 & 0 \\ -2/R_1 & 1 \end{bmatrix} = \begin{bmatrix} A_1 - 2B_1/R_1 & B_1 \\ C_1 - 2D_1/R_1 & D_1 \end{bmatrix} \quad (8)$$

The second propagation step carries the field from the aperture \mathcal{A}_2 at $z_2 = L_0$ through the reflection from the end test mass (ETM) \mathcal{M}_2 to the aperture \mathcal{A}_1 at the reference plane at $z_3 = 2L_0$, the latter of which is coincident with the plane at $z_1 = 0$. The transverse spatial dependence of the field at z_3 is

$$E(x, y, z_1) = \int_{\mathcal{A}_2} dx' dy' \rho_2(x', y') K_{12}(x, y; x', y') E(x', y', L_0) \equiv \hat{K}_{12}[E(x', y', z_2)], \quad (9)$$

where $\rho_2(x, y)$ is the complex reflection coefficient of aperture \mathcal{A}_2 , and the functional form of $K_{12}(x, y; x', y')$ is identical to that of Eq. (6). In this case, the corresponding $ABCD$ matrix elements are given by

$$\begin{bmatrix} A & B \\ C & D \end{bmatrix} = \begin{bmatrix} A_2 & B_2 \\ C_2 & D_2 \end{bmatrix} \cdot \begin{bmatrix} 1 & 0 \\ -2/R_2 & 1 \end{bmatrix} = \begin{bmatrix} D_1 - 2B_1/R_2 & B_1 \\ C_1 - 2A_1/R_2 & A_1 \end{bmatrix}, \quad (10)$$

since $A_2 = D_1$, $B_2 = B_1$, $C_2 = C_1$, and $D_2 = A_1$ in the LIGO standing-wave resonator. Hence, the full round trip through the resonator can be represented by the composite integral transform

$$E(x, y, 0) = \int_{\mathcal{A}_1} dx' dy' \rho_1(x', y') K(x, y; x', y') E(x', y', z_1) \equiv \hat{K}[E(x', y', 0)], \quad (11)$$

where the full round-trip kernel is given by

$$K(x, y; x', y') = \int_{\mathcal{A}_2} dx'' dy'' \rho_2(x'', y'') K_{12}(x, y; x'', y'') K_{21}(x'', y''; x', y'), \quad (12)$$

or $\hat{K}[\cdot] \equiv \hat{K}_{12}[\hat{K}_{21}[\cdot]]$.

We now seek a decomposition of the sideband amplitude function $E_q(\mathbf{r}, t)$ in eigenmodes of the integral transform given by Eq. (11). That is, we wish to identify transverse spatial eigenfunctions $u_{mn}(\mathbf{r})$ that satisfy the linear homogeneous Fredholm equation of the second kind [17]

$$\gamma_{mn} u_{mn}(x, y, 0) = \int_{\mathcal{A}_1} dx' dy' \rho_1(x', y') K(x, y; x', y') u_{mn}(x', y', 0), \quad (13)$$

where the eigenvalue $\gamma_{mn} \equiv |\gamma_{mn}| \exp(-i\varphi_{mn})$ allows us to determine both the round-trip cavity loss $1 - |\gamma_{mn}|^2$ and the round-trip Gouy phase φ_{mn} . The application of the boundary conditions at the apertures to Eq. (4), the Helmholtz equation for an open-sided resonator, generally prevents the propagation kernel given by Eq. (12) from being Hermitian. Hence, the eigenfunctions do *not* generally satisfy the orthonormality relation [15]

$$\int_{\mathcal{A}} dx dy u_{mn}^*(x, y, z) u_{m'n'}(x, y, z) = \delta_{mm'} \delta_{nn'}$$

at any reference plane. Instead, the eigenfunctions are biorthogonal to a related set of functions $v_{mn}(x, y, z)$ that represent fields propagating through the resonator in the *reverse* direction. The corresponding Fredholm integral for these eigenmodes has the form [14]

$$\gamma_{mn} v_{mn}(x, y, 0) = \rho_1(x, y) \int_{\mathcal{A}_1} dx' dy' K^T(x, y; x', y') v_{mn}(x', y', 0), \quad (14)$$

where $K^T(x, y; x', y')$ is the transpose of $K(x, y; x', y')$, and represents the *reverse* round-trip propagation kernel. The fundamental biorthogonality integral

$$\int_{\mathcal{A}_1} dx dy v_{mn}(x, y, 0) u_{m'n'}(x, y, 0) = \int_{-\infty}^{\infty} dx dy v_{mn}(x, y, 0) u_{m'n'}(x, y, 0) = \delta_{mm'} \delta_{nn'} \quad (15)$$

is satisfied discretely (i.e., numerically) for appropriately normalized eigenfunctions, although a rigorous proof has not yet been found. The second integral in Eq. (15) is equivalent to the first, since $v_{mn}(x, y, 0)$ vanishes outside the aperture \mathcal{A}_1 .

Therefore, given the existence of a numerically complete set of forward-propagating transverse spatial eigenfunctions, we can expand the sideband amplitude function as

$$E_q(\mathbf{r}, t) = \sum_{mn} E_{mnq}(z, t) u_{mn}(\mathbf{r}), \quad (16)$$

with a similar expansion for $F_q(\mathbf{r}, t)$. Hence, we can convert Eq. (5) from an integral transform to a simple matrix product with the form

$$E_{mnq}(z_2, t + \tau) = \sum_{m'n'} K_{mn;m'n'}(t) E_{m'n'q}(z_1, t), \quad (17)$$

where τ is the time required by a given wave front to propagate from z_1 to z_2 , and

$$K_{mn;m'n'}(t) = \iint_{-\infty}^{\infty} dx dy \iint_{\mathcal{A}_1} dx' dy' \rho(x', y') v_{mn}(x, y, z_2) K(x, y; x', y'; t) u_{m'n'}(x', y', z_1). \quad (18)$$

The time dependence of $K_{mn;m'n'}(t)$ is determined by the details of the dynamics of the misaligned mirrors.

B. Derivation of the Equation of Motion

1. Discrete iteration

We seek a first-order (in time) evolution equation which predicts the value of the forward-propagating intracavity electric field $E(x, y, 0, t)$ at the reference plane located at $z = 0$ just inside the primary (ITM) mirror. We explicitly allow the positions and alignment angles of the two mirrors to vary with time, and we describe the ITM position by the function $z_1(t) \approx 0$, and the ETM position by $z_2(t) \approx L_0$. We assume that the rates at which these dynamical variables change are small enough that the resulting Doppler shift frequencies are less than the resolution of the interferometer, giving the constraints

$$\dot{z} < \frac{1}{2\pi\mathcal{F}} \frac{\lambda}{\tau_0}, \text{ and}$$

$$\dot{\theta} < \frac{1}{2\mathcal{F}} \frac{\lambda}{\pi w \tau_0},$$

where w is the beam radius at the mirror, \mathcal{F} is the finesse of the resonator, and $\tau_0 \equiv 2L_0/c$. Suppose that at time t the electric field amplitude immediately prior to a reflection from the primary (ITM) mirror position $z_1(t)$ is $E(x, y, 0, t)$. If we follow this phase front to a point just before the reflection from the secondary (ETM) mirror at time $t + L_0/c$, we obtain for the field amplitude $E(x, y, L_0, t + L_0/c)$

$$E(x, y, L_0, t + L_0/c) = \hat{P}_{21}(t)[F(x', y', 0, t)] + \exp[-i2k_0z_1(t)] \hat{K}_{21}(t)[E(x', y', 0, t)], \quad (19)$$

where $\hat{P}_{21}(t)$ is the propagation operator which carries $F(x, y, 0, t)$ from the reference plane just outside \mathcal{M}_1 to the reference plane at z_2 , and $\hat{K}_{21}(t)$, as defined by Eq. (5), is the propagation operator which carries $E(x, y, t)$ from the reference plane at z_1 to the reference plane at z_2 . However, here $\hat{K}_{21}(t)$ includes the effects of the spatial propagation from the ITM to the ETM (described by the $ABCD$ matrix shown in Fig. 2), the reflection from the ITM, and the possible (time-dependent) misalignment of the ITM. If $\hat{K}_{12}(t)$ is the corresponding operator describing propagation from z_2 to z_1 , then again at the reference plane located nominally at z_1 , we have

$$\begin{aligned} E(x, y, 0, t + \tau_0) &= \exp[i2k_0z_2(t + \tau_0/2)] \hat{K}_{12}(t + \tau_0/2)[E(x', y', L_0, t + \tau_0/2)] \\ &= \exp[i2k_0z_2(t + \tau_0/2)] \hat{P}(t)[F(x', y', 0, t)] \\ &\quad + \exp\{i2k_0[z_2(t + \tau_0/2) - z_1(t)]\} \hat{K}(t)[E(x', y', 0, t)], \end{aligned} \quad (20)$$

where $\hat{K}(t)[\] \equiv \hat{K}_{12}(t + \tau_0/2)[\hat{K}_{21}(t)[\]]$ and $\hat{P}(t)[\] \equiv \hat{K}_{12}(t + L_0/c)[\hat{P}_{21}(t)[\]]$. This iterative equation is analytically identical to a discrete time-ordered sum over all prior round-trip propagations of the input field $F(x, y, 0, t)$, which can be written as

$$\begin{aligned} E(x, y, 0, t) &= \sum_{n=1}^{\infty} \exp[i2k_0z_2(t_n + \tau_0/2)] \\ &\quad \times \left\{ \prod_{m=1}^{n-1} \exp\{i2k_0[z_2(t_m + \tau_0/2) - z_1(t_m)]\} \hat{K}(t_m)[\hat{P}(t_m)[F(x', y', 0, t_n)]] \right\}, \end{aligned} \quad (21)$$

where $t_n \equiv t - n\tau_0$.

We obtain a more efficient numerical representation of the intracavity field evolution by expanding both $E(x, y, 0, t)$ and $F(x, y, 0, t)$ as a sum over unperturbed static transverse spatial eigenmodes and distinct sideband frequencies according to Eq. (16). After applying the biorthogonality relation Eq. (15), averaging over a time that is much longer than the largest sideband modulation period, and suppressing the redundant coordinate label for the $z_1 \approx 0$ reference plane, we find

$$\begin{aligned} E_{mnq}(t + \tau_0) &= \exp\{i2k_q[z_2(t + \tau_0/2) - z_1(t)]\} \sum_{m'n'} K_{mn;m'n'}(t) E_{m'n'q}(t) \\ &\quad + \exp[i2k_qz_2(t + \tau_0/2)] \sum_{m'n'} P_{mn;m'n'}(t) F_{m'n'q}(t), \end{aligned} \quad (22)$$

where $k_q \equiv k_0 + \Delta k_q$, $K_{mn;m'n'}(t)$ is given by Eq. (18), and $P_{mn;m'n'}(t)$ is given by a corresponding integral expression. Since $K(x, y; x', y'; t)$ represents propagation over a full round trip through the resonator, in the absence of angular misalignments we have

$$K_{mn;m'n'}(t) = \gamma_{mn} \delta_{mm'} \delta_{nn'} \equiv |\gamma_{mn}| \exp(-i\varphi_{mn}) \delta_{mm'} \delta_{nn'}. \quad (23)$$

In most cases of practical interest, we will be interested in computing the optical response of an aligned, optimized resonator to environmental perturbations. In these cases, the static length of the interferometer will be tuned to maximize the circulating intracavity power of the fundamental carrier spatial mode, giving $2k_0L_0 - \varphi_{00} = 2N\pi$, where N is a large integer. If we write $L(t) \equiv L_0 + \Delta L(t)$, where $\Delta L(t) \approx \lambda_0 = 2\pi/k_0$, then

$$\begin{aligned} \exp\{i[2k_qL(t) - \varphi_{00}]\} &= \exp[i(2k_0L_0 - \varphi_{00})] \exp[i2k_0\Delta L(t)] \\ &\quad \times \exp(i2\Delta\omega_qL_0/c) \exp[i2\Delta k_q\Delta L(t)] \\ &\cong \exp\{i[2k_0\Delta L(t) + \Delta\omega_q\tau_0]\}, \end{aligned} \quad (24)$$

since $\Delta k_q/k_0 \ll 1$. With this simplification, Eq. (22) becomes

$$\begin{aligned} E_{mnq}(t + \tau_0) &= \exp\{i[2k_0\Delta L(t) + \Delta\omega_q\tau_0]\} \left[\sum_{m'n'} K_{mn;m'n'}(t) E_{m'n'q}(t) \right. \\ &\quad \left. + \exp[i2k_0z_1(t)] \sum_{m'n'} P_{mn;m'n'}(t) F_{m'n'q}(t) \right]. \end{aligned} \quad (25)$$

or equivalently

$$\mathbf{E}_q(t + \tau_0) = \exp \{i [2k_0 \Delta L(t) + \Delta \omega_q \tau_0]\} \{ \mathbf{K}(t) \cdot \mathbf{E}_q(t) + \exp [i 2k_0 z_1(t)] \mathbf{P}(t) \cdot \mathbf{F}_q(t) \}, \quad (26)$$

where $\mathbf{E}_q(t)$ and $\mathbf{F}_q(t)$ are vectors and $\mathbf{K}(t)$ and $\mathbf{P}(t)$ are square matrices with the same dimensionality. Eq. (26) can be used to forward-step the intracavity field at one round trip per step. Note that Eq. (26) reduces to the static modal model [12] when *all* dynamic variables are constant and $\mathbf{E}_q(t + \tau_0) = \mathbf{E}_q(t)$, providing an indication that both resonant and nonresonant (i.e., small-signal and large-signal) phenomena have been included in its formulation.

In some cases, the dynamic variables (i.e., the mirror degrees of freedom and/or the input field) may be varying slowly enough that we don't need to update them prior to every iteration. For a relatively small number of consecutive steps, we can simply apply Eq. (26) consecutively until we detect that one of the field components has changed by more than a preset threshold. However, if the number of steps to be taken is potentially very large, then we can be more efficient by diagonalizing \mathbf{K} and summing the iteration directly. Suppose that, in some basis \mathbf{S} , the matrix operator \mathbf{K} can be diagonalized as $\mathbf{K} = \mathbf{S} \Lambda \mathbf{S}^{-1}$, where Λ is the diagonal eigenvalue matrix. Then, treating F , z_1 , z_2 , \mathbf{P} , and \mathbf{K} as constants, Eq. (26) gives

$$\mathbf{E}_q(t + n \tau_0) \cong \mathbf{S} \cdot \left\{ \mathbf{D}^n \cdot \mathbf{S}^{-1} \cdot \mathbf{E}_q(t) + \beta \frac{1 - \mathbf{D}^n}{1 - \mathbf{D}} \cdot \mathbf{S}^{-1} \cdot \mathbf{P} \cdot \mathbf{F}_q \right\}, \quad (27)$$

where $\mathbf{D} \equiv \exp \{i [2k_0 \Delta L + \Delta \omega_q \tau_0]\} \Lambda$, $\beta \equiv \exp \{i [2k_0 \Delta z_2 + \Delta \omega_q \tau_0]\}$, and $\Delta z_2 \equiv z_2 - L_0$.

2. Continuous evolution

It is tempting to assume that the round-trip time τ_0 is sufficiently brief that we can expand the left-hand side of Eq. (26) in a Taylor series about the time t , thereby obtaining a first-order linear ordinary differential equation that describes the evolution of the electric field amplitude at the reference plane $z = 0$:

$$\begin{aligned} \tau_0 \dot{\mathbf{E}}_q(t) = & - \{1 - \exp \{i [2k_0 \Delta L(t) + \Delta \omega_q \tau_0]\} \mathbf{K}(t)\} \cdot \mathbf{E}_q(t) \\ & + \exp \{i [2k_0 \Delta z_2(t) + \Delta \omega_q \tau_0]\} \mathbf{P}(t) \cdot \mathbf{F}_q(t), \end{aligned} \quad (28)$$

where $\Delta z_2(t) \equiv z_2(t) - L_0$. As it stands, Eq. (28) is a reasonably efficient ODE which provides numerically stable solutions for the intracavity electric field when used with adaptive-stepsize methods to describe those cases where the mirror dynamic variables are sufficiently slowly varying relative to the cavity round-trip time. We can relax the latter constraint somewhat, and enable Eq. (28) to treat accurately systems moving rapidly in z , if we add the constraint that the interferometer operates near a resonance. In this case, we can approximate the sum in Eq. (21) as an integral, and differentiate the resulting equation by t . If the mirror misalignment angles change slowly enough that $\mathbf{K}(t)$ does not vary significantly during the cavity storage time $\tau_c \equiv \tau_0 / 2 \ln(1/|\varphi_{00}|)$, then in this continuum limit

$$\begin{aligned} \tau_0 \dot{\mathbf{E}}_q(t) = & \left\{ -\frac{\tau_0}{2\tau_c} + i [2k_0 \Delta L(t) + \Delta \omega_q \tau_0] + \ln \mathbf{K}(t) \right\} \cdot \mathbf{E}_q(t) \\ & + \exp \{i [2k_0 \Delta z_2(t) + \Delta \omega_q \tau_0]\} \mathbf{P}(t) \cdot \mathbf{F}_q(t). \end{aligned} \quad (29)$$

As a test of our method, consider the experiment performed by An *et al.*, [18] where a constant TEM₀₀ input field was mode-matched into a Fabry-Perot interferometer while the mirror \mathcal{M}_2 was moved with a constant velocity v . In this case, no sidebands were added to the fundamental laser frequency, the length of the resonator was only 1 mm (resulting in a round-trip time $\tau_0 \cong 7$ ps), and the cavity finesse was approximately 10^6 . The alignment of each mirror was tightly mechanically controlled, so that only the fundamental TEM₀₀ transverse mode oscillated within the resonator. Since $\Delta L(t) = vt$, we can rewrite Eq. (29) as

$$\dot{E}_{00}(t) = - \left(\frac{1}{2\tau_c} + i \frac{t}{T_m^2} \right) E_{00}(t) + 1, \quad (30)$$

where we have defined $T_m^2 \equiv \lambda \tau_0 / 4\pi v$ and chosen the amplitude of F_{00} to simplify subsequent calculations. In this simple form, it is clear that the experimental dynamics are simply those of a damped resonator with a linearly chirped instantaneous frequency, caused by the overlap of the phase of a given round trip with that of the previous trip. Contrary to the interpretation of An *et al.*, Doppler effects — which we have explicitly ignored in our analysis — play no significant role in this experiment. [19] We can integrate Eq. (30) analytically to obtain

$$E_{00}(t) = \frac{1-i}{2} T_m \exp[\zeta^2(t)] \left\{ \sqrt{\pi} [\operatorname{erf} \zeta(t) - \operatorname{erf} \zeta(t_0)] - \frac{\exp[-\zeta^2(t_0)]}{\zeta(t_0)} \right\}, \quad (31)$$

where we have set the initial value of the intracavity field to the steady-state value $E_{00}(t_0) = (1/2\tau_c - it_0/T_m^2)^{-1}$, and

$$\zeta(t) \equiv \frac{1+i}{2T_m} \left(t + i \frac{T_m^2}{2\tau_c} \right).$$

We have computed $E_{00}(t)$ for $T_m = 0.12 \mu\text{s}$ and $T_m = 0.26 \mu\text{s}$, and graphed the results in Fig. 3 and Fig. 4, respectively. The agreement with the work of An *et al.* — who truncated an infinite series to numerically compute their theoretical curves — is quantitatively excellent, even though we have assumed that the injected laser field was perfectly monochromatic.

Nevertheless, Eq. (29) *cannot* be used to describe the field evolution at the exact midpoint between two resonant frequencies, since the steady-state solution it provides there differs substantially from the correct value predicted by Eq. (26). Our simulation of the LIGO interferometer relies heavily on sideband fields that are antiresonant in the Fabry-Perot interferometers, and therefore we would surrender considerable accuracy using Eq. (29) to describe these modes. Furthermore, we lose periodicity when we pass from the discrete case to the continuum limit, necessitating the ad hoc addition of adjacent longitudinal modes in situations where the separation of the mirrors changes by more than λ_0 . In practice, then, we can use Eq. (26) to determine the fields when the dynamic variables are relatively rapidly varying, and either Eq. (27) or Eq. (28) when they are relatively slowly varying. For modes which are also nearly resonant, we can employ Eq. (29).

C. Small-Angle Hermite-Gauss Approximation

If we find that the eigenmodes $u_{mn}(\mathbf{r})$ — and the corresponding biorthogonal functions $v_{mn}(\mathbf{r})$ — are numerically complete, then we can reduce the round-trip propagation matrix $\mathbf{K}(t)$ to a product of the four matrices $\mathbf{M}_1(t)$, \mathbf{G}_{21} , $\mathbf{M}_2(t)$, and \mathbf{G}_{12} , which respectively represent [12]

1. propagation from the reference plane z_1 , followed by the prompt reflection from the mirror \mathcal{M}_1 ;
2. the propagation step from z_1^+ to the reference plane at z_2 ;
3. the prompt reflection from the mirror \mathcal{M}_2 ; and
4. the propagation step from z_2^+ to the reference plane at z_1 .

Construction of the matrices representing free-space propagation for the LIGO Fabry-Perot interferometer is straightforward in principle, using Eq. (6) and Eq. (18) with $A = D = 1$, $B = L_0$, and $C = 0$.

Since the $ABCD$ matrix describing reflection from a mirror near normal incidence has elements $A = D = 1$, $B = 0$, and $C = -2/R$, we must use the appropriate limiting form of Eq. (6) to define the propagator:

$$\lim_{B \rightarrow 0} K(x, y; x', y') = \frac{\delta(x' - x/A) \delta(y' - y/A)}{|A|} \exp \left[\frac{\pi}{\lambda} AC (x'^2 + y'^2) \right] \quad (32)$$

As described in section III A 1, a misalignment of a mirror by the angles $\Delta\theta_x$ and $\Delta\theta_y$ about the y and x cartesian axes, respectively, rotates the incident wave vector \mathbf{k} by an amount $\Delta\mathbf{k} = 2\Delta\theta_x \hat{\mathbf{x}}' + 2\Delta\theta_y \hat{\mathbf{y}}'$, and reorients the wave front of the reflected field. The corresponding propagator has the form

$$M(x, y; x', y'; \Delta\theta_x, \Delta\theta_y) = \delta(x' - x) \delta(y' - y) \exp \left\{ ik \left[2(x \Delta\theta_x + y \Delta\theta_y) - \frac{x'^2 + y'^2}{R} \right] \right\}. \quad (33)$$

As a practical analytical example, consider the special case where the mirror apertures are large compared to the beam spot diameters at the mirrors, and the misalignment angles are small compared to the beam expansion half-angle. Then the sets of Hermite-Gauss eigenmodes described by Eq. (A4) and the corresponding equation for $u_{mn}(x, y, L_0)$ are each approximately complete, and the mirror-to-mirror propagation matrices \mathbf{G}_{21} and \mathbf{G}_{12} can be easily expressed in terms of the Gouy phase given by Eq. (A5). In the Hermite-Gauss basis, we can write both \mathbf{G}_{21} and \mathbf{G}_{12} as

$$\mathbf{G}_{21} = \mathbf{G}_{12} \equiv g_0 \mathbf{G}_0 \quad (34)$$

where the elements of \mathbf{G}_0 are [15]

$$\mathbf{G}_{0m'n';mn} \equiv g_0^{m+n} \delta_{mm'} \delta_{nn'}, \text{ and} \quad (35)$$

$$g_0 \equiv \exp(-i\varphi_{00}/2) = \exp(-i \cos^{-1} \sqrt{g_1 g_2}) = \sqrt{g_1 g_2} - i \sqrt{1 - g_1 g_2}. \quad (36)$$

For the purposes numerical efficiency and accuracy, we precalculate the analytic matrix elements of Eq. (33) at the reference plane z (located at either mirror), using the integral equation

$$\begin{aligned} \mathbf{M}_{m'n';mn}(t) &\equiv \int_{-\infty}^{\infty} dx dy \int_{-\infty}^{\infty} dx' dy' \rho(x', y') \\ &\quad \times v_{mn}(x, y, z^+) u_{m'n'}(x, y, z^-) M(x, y; x', y'; \Delta\theta_x, \Delta\theta_y) \\ &\equiv -r \tilde{M}_{mm'}[\Theta_x(t)] \tilde{M}_{nn'}[\Theta_y(t)], \end{aligned} \quad (37)$$

where r is the amplitude reflection coefficient of the mirror, $\Theta_x(t) \equiv \theta_x(t)/(\lambda/\pi w)$, $\Theta_y(t) \equiv \theta_y(t)/(\lambda/\pi w)$, and

$$\begin{aligned} \tilde{M}_{mm'}(\Theta_x) &\equiv \left[\frac{1}{2^{m'+m} m'! m! \pi w^2} \right]^{\frac{1}{2}} \int_{-\infty}^{\infty} dx H_{m'} \left(\frac{\sqrt{2}x}{w} \right) H_m \left(\frac{\sqrt{2}x}{w} \right) \\ &\quad \times \exp \left[-2 \left(\frac{x}{w} \right)^2 + i 4 \left(\frac{x}{w} \right) \Theta_x \right], \end{aligned} \quad (38)$$

with a similar expression for $\tilde{M}_{nn'}(\Theta_y)$. Here, the notations $u_{mn}(x, y, z^-)$ and $v_{mn}(x, y, z^+)$ indicate that both the forward-propagating and reverse-propagating eigenfunctions must be evaluated *prior* to reaching the reflecting surface of the mirror.

As an example, consider the calculation of the mirror misalignment matrix for the case $m+n \leq 1$. Using Eq. (37), we obtain

$$\mathbf{M}(t) = \exp \{ -2[\Theta_x^2(t) + \Theta_y^2(t)] \} \begin{bmatrix} 1 & i2\Theta_x(t) & i2\Theta_y(t) \\ i2\Theta_x(t) & 1 - 4\Theta_x^2(t) & -4\Theta_x(t)\Theta_y(t) \\ i2\Theta_y(t) & -4\Theta_x(t)\Theta_y(t) & 1 - 4\Theta_y^2(t) \end{bmatrix}. \quad (39)$$

Thus, we can use either Eq. (26) or Eq. (28), with

$$\mathbf{K}(t) = r_1 r_2 \mathbf{G}_0 \mathbf{M}_2(t + \tau_0/2) \mathbf{G}_0 \mathbf{M}_1(t), \text{ and} \quad (40a)$$

$$\mathbf{P}(t) = -i t_1 r_2 \mathbf{G}_0 \mathbf{M}_2(t + \tau_0/2) \mathbf{G}_0, \quad (40b)$$

where we have adopted the standard laser-industry phase convention [15] that models a mirror as a quarter-wave stack. Hence, reflection multiplies an incident field by $-r$, and transmission by it , regardless of the direction of incidence.

A numerical example of the utility of this approach is shown in Fig. 5, for the case of a LIGO Fabry-Perot interferometer with the properties described in Appendix A and characteristics listed in table I. Here, $\Delta L(t) = 0$, and beginning at time $t = 0$ the ETM oscillates about the y -axis with amplitude $\Theta_m = 0.01$ and period $2\pi/\omega_{2x} = 100\tau_0$:

$$\begin{aligned} \Theta_{2x} &= \Theta_m \sin(\omega_{2x} t), \\ \Theta_{1x} &= \Theta_{1y} = \Theta_{2y} = 0. \end{aligned}$$

We have assumed that the only nonvanishing component of the input field is TEM_{00} , and we analyze the carrier wave only; i.e., $F_{000} = 1$ (corresponding to an input power of 1 W), and all other F_{mnq} coefficients are zero. We have shown the time evolution of the real and imaginary parts of the TEM_{01} at the reference plane just inside the ITM. Prior to the onset of oscillation at $t = 0$, the cavity has been loaded so that $E_{000} = F_{000}/(1 - r_1 r_2)$. Although this result has been obtained using Eq. (26), we obtain a virtually identical output from Eq. (28), implemented with a simple Cash-Karp numerical ODE integration scheme. [20]

III. THE LIGO INTERFEROMETER

Figure 6 is a schematic diagram of the primary optical components, electric fields, and conventions used in the LIGO interferometer (historically denoted ‘‘IFO’’) simulation. The coordinate systems for all fields propagating to the right or downward are right-handed, while those for propagation to the left or upward are left-handed. (The unit vector $\hat{\mathbf{z}}$ is always parallel with the direction of propagation, and $\hat{\mathbf{y}}$ is always directed towards the reader.) All angular rotation axes are defined so that a positive mirror misalignment causes the propagation vector — reflecting from the vacuum-coating interface of the mirror — to deflect away from the z axis in the positive direction.

A. The IFO Power Recycler Coupling Equations

1. The adiabatic approximation

Prior to deriving the equations that connect the two FPIs through the recycling cavity, we make two simplifying assumptions:

1. *The adiabatic approximation is valid.* The round-trip time delay in the recycling cavity is almost 500 times smaller than the round-trip time delay in either FPI. Therefore, provided that no significant mechanical perturbations in the power-recycling cavity occur on time scales smaller than approximately 100 ns, the time-dependent coupling equations can be approximated by steady-state linear equations that connect the electromagnetic fields in the two FPIs.
2. *We assume that all of the resonators are nearly perfectly mode-matched.* If this assumption is satisfied, then the TEM_{mn} output mode emerging from one FPI will propagate through the power recycling cavity and accurately match the corresponding TEM_{mn} input mode incident on the other FPI. The curvature of any TEM_{mn} mode emerging from either FPI and incident on the recycling mirror matches that of the recycling mirror. The residual mode-mismatches that result from the misalignment of any mirror in the system are fully described by the corresponding mirror matrix operator. However, if this assumption is violated, then we must include additional matrix operators which describe imperfect coupling between the fields circulating in the recycling cavity and those stored in the FPIs. This is a relatively straightforward task to complete (particularly in software), but it would significantly complicate our subsequent presentation.

For reference, the optical parameters and operating characteristics of the components of the LIGO IFO power recycling cavity are listed in table II. Note that the computations of the geometric optical characteristics assume that the Hermite-Gauss approximation is valid. The recycling cavity is only marginally stable, with a stability factor of $g_1 g_5 = 0.999994$. The common-mode free spectral range is $\Delta\nu_L = 16$ MHz, corresponding to a round-trip time of 63 ns. The common-mode single-pass TEM_{00} Gouy phase is $\cos^{-1} \sqrt{g_1 g_5} = 0.138^\circ$, corresponding to a Gouy frequency shift of $\Delta\nu_G = 12.2$ kHz.

We assume that the IFO beamsplitter can be treated as a mirror with $r \cong t \cong 1/\sqrt{2}$, and that it is suspended in much the same fashion as the power recycling mirror or any of the FPI end mirrors: we can describe the angular misalignments of the body axes using the two infinitesimal angles $\Delta\theta_x$ and $\Delta\theta_y$, and the beamsplitter can move a distance Δz along the center surface normal. Reflection in the case of perfect alignment transforms the right-handed coordinate system $\{\hat{\mathbf{x}}, \hat{\mathbf{y}}, \hat{\mathbf{z}}\}$ of the incident field into the left-handed coordinate system $\{\hat{\mathbf{x}}', \hat{\mathbf{y}}', \hat{\mathbf{z}}'\}$ of the reflected field. In the latter coordinate system, a misaligned mirror nominally at normal incidence rotates the reflected wavevector by an amount

$$\Delta \hat{\mathbf{k}}' \equiv \hat{\mathbf{k}}' - \hat{\mathbf{k}} = 2 \Delta\theta_x \hat{\mathbf{x}}' + 2 \Delta\theta_y \hat{\mathbf{y}}', \quad (41)$$

as expected, while for the beamsplitter we find

$$\Delta \hat{\mathbf{k}}' = 2 \Delta\theta_x \hat{\mathbf{x}}' + \sqrt{2} \Delta\theta_y \hat{\mathbf{y}}'. \quad (42)$$

Therefore, when we use the propagation operator Eq. (33) to represent a misaligned beamsplitter, we must replace $\Delta\theta_y \rightarrow \Delta\theta_y/\sqrt{2}$.

Throughout our model, we adopt the laser-industry convention that a dielectric-coated mirror can be represented as a quarter-wave stack. Then each mirror has direction-independent amplitude reflection and transmission coefficients of $-r$ and it , respectively, where r^2 and t^2 are the corresponding intensity reflectance and transmittance. [15] In principle, we can treat the beamsplitter in the same fashion. In practice, however, we must tune the microscopic position of the beamsplitter so that the carrier electromagnetic field at the antisymmetric port is zero when the entire interferometer is perfectly aligned and the Michelson arms have equal length. Hence, we require another phase shift of π in the power recycling cavity to compensate for the π phase shift the carrier experiences upon reflection from either FPI. We accomplish this by adjusting the position of the beamsplitter by a distance $\Delta z = \pi/2\sqrt{2}k = \lambda/4\sqrt{2}$. In effect, then, the front and back reflection coefficients of the beamsplitter become $+ir$ and $-ir$, respectively, while the transmission coefficient remains it for all possible transmission directions.

Under these assumptions, the matrix operators which describe propagation between the various reference planes shown in Fig. 6 are given by table III. The propagator in the first column of table III can be constructed explicitly by multiplying the product of the matrix operators listed in the fourth column by the product of the scalar coefficient listed in the second column and $\exp(i\varphi)$, where φ is the entry in the third column. For example,

$$\hat{K}_{15} = -ir_5 t_6 \exp \{i [\omega_q (\tau_C + \tau_D) / 2 - 4\Delta\pi z_5]\} \hat{G}_{16} \hat{G}_{65} \hat{M}_5. \quad (43)$$

The operator \hat{K}_{kj} describes reflection from mirror \mathcal{M}_j followed by propagation to the reference plane at mirror \mathcal{M}_k , while \hat{P}_{kj} describes transmission through \mathcal{M}_j followed by propagation to the reference plane at \mathcal{M}_k . (The index $j = 7$ is used to denote the detector at the antisymmetric port.) Here r_j and t_j are respectively the amplitude reflection and transmission coefficients of mirror \mathcal{M}_j , Δz_j is the residual position shift of \mathcal{M}_j in units of the laser wavelength λ_0 , ω_q is the angular frequency of the RF sideband q , and $\tau_C \equiv 2l_C/c$ and $\tau_D \equiv 2l_D/c$, where l_C and l_D are the common and differential arm distances, respectively. The mirror operator \hat{M}_j represents mode-mixing due to reflection from the front (i.e., the vacuum-coating interface) of mirror \mathcal{M}_j , while $\hat{M}_j^\dagger \equiv \hat{M}_j^{*T}$ represents reflection through the substrate of \mathcal{M}_j . The Gouy operator \hat{G}_{kj} describes free-space propagation from \mathcal{M}_j to \mathcal{M}_k . In practice, we ignore the slight difference in length between the two arms of the IFO when we compute the corresponding Gouy shifts, and we set $\hat{G}_{16} = \hat{G}_{61} = \hat{G}_{36} = \hat{G}_{63}$. Also, for convenience, we set $\hat{G}_{56} = \hat{G}_{65} = \hat{G}_{76} = \hat{G}_{67}$.

Under the assumptions listed above, and using Fig. 6 and table III, we can easily calculate the electric field at the reference plane just inside the power recycling mirror \mathcal{M}_5 in terms of the input laser field F_5 and the two fields emerging from the FPIs. Suppose that we have just updated the FPI intracavity fields E_1 and E_2 . Then the corresponding value of E_5 is

$$E_5 = \frac{(\hat{P}_{5115} + \hat{P}_{5225}) F_5 + \hat{P}_{51} E_1 + \hat{P}_{52} E_2}{1 - (\hat{K}_{5115} + \hat{K}_{5335})} \quad (44)$$

where we have defined the round-trip recycling-cavity operators

$$\hat{K}_{5115} \equiv \hat{K}_{51} \hat{K}_{15}, \quad (45a)$$

$$\hat{K}_{5225} \equiv \hat{K}_{52} \hat{K}_{25}, \quad (45b)$$

$$\hat{P}_{5115} \equiv \hat{K}_{51} \hat{P}_{15}, \quad (45c)$$

$$\hat{P}_{5225} \equiv \hat{K}_{52} \hat{P}_{25}. \quad (45d)$$

Once this reference field has been calculated, we can update the FPI input fields prior to the next iteration:

$$F_1 = \hat{K}_{15} E_5 + \hat{P}_{15} F_5, \quad (46a)$$

$$F_2 = \hat{K}_{25} E_5 + \hat{P}_{25} F_5. \quad (46b)$$

Finally, we can determine the output field at the antisymmetric port using the input and intracavity fields at the FPI ITM reference planes:

$$E_7 = \hat{P}_{71} E_1 + \hat{P}_{72} E_2 + \hat{K}_{71} F_1 + \hat{K}_{72} F_2. \quad (47)$$

In the Hermite-Gauss approximation and the steady-state case, some patient simplification shows that our model reduces to the modal representation of Hefetz *et al.* [12], as required.

B. Signal Demodulation

As discussed in section IV, one of the most important applications of models of the optical response of the LIGO interferometer to environmental perturbations is the construction of computational tests of servo-control locking schemes. In this case, we must develop a representation of the detectors used to convert LIGO optical signals to electrical signals processed by the control systems. In order to optimize the power-recycling gain, a control system must position the beamsplitter such that the antisymmetric port is set on a dark fringe (minimum of the light power). However, this condition makes it impossible to measure small differential length deviations without adding other light frequencies. LIGO implements a frontal modulation scheme where phase-modulated radio-frequency (RF) sidebands are imposed on the incoming light beam [6]. Because of the macroscopic asymmetry in the Michelson arm lengths, these RF sidebands are shifted away from the dark fringe and, therefore, can have a significant coupling to the antisymmetric port. Away from the exact dark fringe condition the carrier leakage field beats against the RF sideband fields, producing a beat signal which amplitude is proportional to the differential length deviation [21].

Let the real column vectors $\mathbf{E}_0(t)$, $\mathbf{E}_{+q}(t)$, and $\mathbf{E}_{-q}(t)$ represent the components of the electric field, in some spatial basis measured at a particular reference plane at time t , at the optical carrier frequency ω_0 and the RF modulation

frequencies $+\Delta\omega_q$ and $-\Delta\omega_q$, respectively. Then, at a new reference plane with relative fundamental Gouy shift φ_{00} , the total electric field can be written as

$$\mathbf{E}(\varphi_{00}; t) = \text{Re} \{ G(\varphi_{00}) [\mathbf{E}_0(t) + \mathbf{E}_{+q}(t) \exp(-i\Delta\omega_q t) + \mathbf{E}_{-q}(t) \exp(+i\Delta\omega_q t)] \exp(-i\omega_0 t) \}, \quad (48)$$

where $G(\varphi_{00})$ is the Gouy matrix operator representing free-space propagation between the two reference planes, with elements

$$G_{m'n';mn}(\varphi_{00}) \equiv \exp[-i(m+n)\varphi_{00}] \delta_{mm'} \delta_{nn'} \quad (49)$$

in the Hermite-Gauss TEM_{mn} basis.

Consider a detector \mathcal{D}_1 placed at the new reference plane, with a real symmetric matrix operator representation D in the basis chosen for the electric field Eq. (48). The real RF demodulated signal $S(\varphi_{00}; t)$ produced by the detector is then

$$S(\varphi_{00}; t) = \mathbf{E}^T(\varphi_{00}; t) D \mathbf{E}(\varphi_{00}; t). \quad (50)$$

Substituting Eq. (48) into Eq. (50) and ignoring terms corresponding to DC, optical, and RF second harmonic frequencies yields

$$\begin{aligned} \bar{S}(\varphi_{00}; t) = \text{Re} \left\{ \mathbf{E}_0^\dagger(t) \tilde{D}(\varphi_{00}) [\mathbf{E}_{+q}(t) + \mathbf{E}_{-q}(t)] \cos(\Delta\omega_q t) \right\} \\ - \text{Re} \left\{ \mathbf{E}_0^\dagger(t) \tilde{D}(\varphi_{00}) [\mathbf{E}_{+q}(t) - \mathbf{E}_{-q}(t)] i \sin(\Delta\omega_q t) \right\}. \end{aligned} \quad (51)$$

where $\tilde{D}(\varphi_{00}) \equiv G^\dagger(\varphi_{00}) D G(\varphi_{00})$.

We can simplify Eq. (51) further by fixing the phase of the RF modulation. We assume that the physical process used to modulate the phase of the laser electric field input to the interferometer follows the cosine function, and we seek the corresponding quadrature components of $\bar{S}(\varphi_{00}; t)$ according to

$$\bar{S}(\varphi_{00}; t) \equiv S_I(\varphi_{00}; t) \cos(\Delta\omega_0 t) + S_Q(\varphi_{00}; t) \sin(\Delta\omega_0 t) \quad (52)$$

If we write the cosine phase modulation function as a Bessel function expansion, keeping only the DC and first-harmonic terms (a good approximation for modulation depths satisfying $\beta \ll 1$)

$$\begin{aligned} \exp[-i\beta \cos(\Delta\omega_0 t)] &= \sum_{n=-\infty}^{\infty} i^{-n} J_n(\beta) \exp(-in\Delta\omega_0 t) \\ &\cong J_0(\beta) - iJ_1(\beta) \exp(-i\Delta\omega_0 t) - iJ_1(\beta) \exp(+i\Delta\omega_0 t), \end{aligned} \quad (53)$$

then we can express the quadrature components of $\bar{S}(\varphi_{00}; t)$ as

$$S_I(\varphi_{00}; t) = \text{Im} [V_{+q}(\varphi_{00}; t) + V_{-q}(\varphi_{00}; t)], \quad (54a)$$

$$S_Q(\varphi_{00}; t) = \text{Re} [V_{+q}(\varphi_{00}; t) - V_{-q}(\varphi_{00}; t)], \quad (54b)$$

where we have defined the reduced field amplitudes

$$\tilde{\mathbf{E}}_0(t) \equiv \mathbf{E}_0(t) / J_0(\beta), \quad (55a)$$

$$\tilde{\mathbf{E}}_{\pm q}(t) \equiv i\mathbf{E}_{\pm q} / J_1(\beta), \quad (55b)$$

and the auxiliary variables

$$V_{\pm q}(\varphi_{00}; t) \equiv J_0(\beta) J_1(\beta) \tilde{\mathbf{E}}_0^\dagger(t) \tilde{D}(\varphi_{00}) \tilde{\mathbf{E}}_{\pm q}(t). \quad (56)$$

Then the complex envelope function $\tilde{S}(\varphi_{00}; t)$ of the signal

$$\bar{S}(\varphi_{00}; t) = \text{Re}[\tilde{S}(\varphi_{00}; t) \exp(-i\Delta\omega_0 t)]$$

has the simple computational form

$$\tilde{S}(\varphi_{00}; t) \equiv S_I(\varphi_{00}; t) + iS_Q(\varphi_{00}; t) = i [V_{-q}^*(\varphi_{00}; t) - V_{+q}(\varphi_{00}; t)], \quad (57)$$

where

$$S_I(\varphi_{00}; t) = \text{Im} [V_{+q}(\varphi_{00}; t) + V_{-q}(\varphi_{00}; t)], \quad (58a)$$

$$S_Q(\varphi_{00}; t) = -\text{Re} [V_{+q}(\varphi_{00}; t) - V_{-q}(\varphi_{00}; t)]. \quad (58b)$$

The matrix elements of the detection operator (in the $\{x, y\}$ basis of the electromagnetic field) are given by

$$D_{m'n';mn} \equiv \int_{-\infty}^{\infty} dx dy v_{mn}(x, y) u_{m'n'}(x, y) \hat{D}(x, y). \quad (59)$$

If $\hat{D}(x, y)$ is a full-plane detector, then the matrix representing the detection operator is simply the identity matrix. However, if $\hat{D}(x, y)$ is split along the y -axis and the signals from the two resulting half-planes are subtracted, then Eq. (59) takes the form

$$D_{m'n';mn} \equiv \int_{-\infty}^{\infty} dy \left(\int_0^{\infty} dx - \int_{-\infty}^0 dx \right) v_{mn}(x, y) u_{m'n'}(x, y). \quad (60)$$

In practice, in some known basis we can compute separately the corresponding one-dimensional matrices for full-plane and split-plane detectors ($D_{x;m',m}$ and $D_{y;n',n}$), and then explicitly construct the corresponding two-dimensional matrix using the composition rule

$$D_{m'n';mn} = D_{x;m',m} D_{y;n',n} \quad (61)$$

For example, in the small-angle Hermite-Gauss case, the split-plane detector operators D_x and D_y both have the form

$$D = \sqrt{\frac{\pi}{2}} \begin{pmatrix} 0 & 1 & 0 & & \\ 1 & 0 & \frac{1}{\sqrt{2}} & \cdots & \\ 0 & \frac{1}{\sqrt{2}} & 0 & & \\ & \vdots & & \ddots & \\ & & & & \ddots \end{pmatrix} \quad (62)$$

In this way, we can build full-plane, x -oriented and y -oriented split-plane, and quad-plane detector matrices.

The resonant and nonresonant frequencies ($\omega_r = 2\pi \times 23.970592332977$ MHz and $\omega_{nr} = 2\pi \times 35.955888499466$ MHz, respectively) have been chosen explicitly to provide

$$\begin{aligned} \exp(i\omega_r\tau_0) &= \exp(i\omega_{nr}\tau_0) = -1, \text{ and} \\ \exp(i\omega_r\tau_C) &= \exp(i\omega_{nr}\tau_C) = \pm i. \end{aligned}$$

IV. RESULTS AND CONCLUSIONS

As an example, we study the effects of alignment errors on the demodulated signal at the antisymmetric port. Fig. 7 shows the simulation of a constant velocity scan of the in-line arm cavity rear mirror. The length of the off-line arm cavity, the length of the power recycling cavity and the Michelson length were held constant on resonance and at the dark fringe, respectively, during the simulation. The scan interval was chosen so that the resonance of the in-line arm cavity appears at the center of the plot range. In the first simulation (solid curve) the interferometer was perfectly aligned, whereas during the second simulation a static misalignment angle of $2 \mu\text{rad}$ was applied to the scanning mirror. A signal degradation of about 50% can be observed in the misaligned case, illustrating the tight requirement for initial alignment in LIGO.

We are currently working on generalizing this result to other degrees-of-freedom by calculating the alignment tolerance for other mirrors, and by investigating the effects of alignment errors if neither of the two arm cavities is near resonance [22]. This will allow us to determine exactly how well the interferometer has to be aligned before the cavities can be brought into resonance.

We conclude that this spatiotemporal model is well suited for studying optical transient phenomena in LIGO-type detectors, and for investigating the dynamical effects of environmental perturbations of the position and orientation of optical components on intracavity fields. In this work special emphasis was placed on a general mathematical derivation of the modal equations from basic optical principles, and on justifying all necessary approximations. If large-angle misalignments of the intracavity optics must be studied, then only the propagation and detector matrices must be recomputed using a more accurate biorthogonal eigenmode basis set that takes proper account of the intracavity losses; all other aspects of our formalism remain unaltered.

The techniques developed in the present work are general enough that they can be readily applied to other long-baseline laser interferometer configurations, such as gravitational wave detectors deploying dual recycling.

ACKNOWLEDGMENTS

We are grateful to Hiro Yamamoto for reading the LIGO technical documents upon which this paper is based, and for performing preliminary tests of the simulation codes. We thank Martin Zwickel for helping with the simulations, and we appreciate the many useful discussions we had with our colleagues of the LIGO project. This work is supported by NSF grant PHY-9210038.

APPENDIX A

The operating characteristics of the FPI shown in Fig. 1 can be derived using either the partial differential equation Eq. (4) or the two-dimensional integral equation Eq. (5). [15] First, we define the stability parameters

$$g_1 \equiv A - \frac{n_1 B}{R_1}, \quad (\text{A1a})$$

$$g_2 \equiv D - \frac{n_2 B}{R_2}, \quad (\text{A1b})$$

where R_j is the radius of mirror \mathcal{M}_j , and n_j is the refractive index of the medium in contact with \mathcal{M}_j . (Note that $R_j > 0$ for concave mirrors, and $R_j < 0$ for convex mirrors.) Stable operation of the FPI requires that the stability factor $g_1 g_2$ satisfies the condition $0 \leq g_1 g_2 \leq 1$. Then, in the case where the mirror apertures are infinite, we can compute the root-mean-square beam radii of the lowest-order modes at the positions of the end mirrors using the expressions

$$\frac{\pi w_1^2}{\lambda} = B \sqrt{\frac{g_2}{g_1(1 - g_1 g_2)}}, \quad (\text{A2a})$$

$$\frac{\pi w_2^2}{\lambda} = B \sqrt{\frac{g_1}{g_2(1 - g_1 g_2)}}. \quad (\text{A2b})$$

Finally, the far-field beam expansion half-angle at either mirror is given by

$$\Delta\theta_j = \frac{\lambda}{\pi w_j} \sqrt{1 + \left(\frac{\pi n_j w_j^2}{\lambda R_j} \right)^2}. \quad (\text{A3})$$

Note that we have constructed Eq. (A3) as a function of field parameters known at the position of mirror \mathcal{M}_j , without referring directly to the size of the beam waist radius w_0 . Whenever the $ABCD$ matrix elements represent a relatively complicated sequence of optical elements, the waist position and size not only may be difficult to calculate, but also may not directly determine the beam expansion angles at the mirrors.

Once w_1 is known, the corresponding general transverse field at the position $z_1 = 0$ for the cylindrically symmetric infinite-aperture case can be expressed as a linear superposition of the Hermite-Gauss eigenmodes

$$u_{mn}(x, y, 0) = \left[\frac{1}{2^{m+n} m! n! \pi w_1^2} \right]^{\frac{1}{2}} H_m \left(\frac{\sqrt{2}x}{w_1} \right) H_n \left(\frac{\sqrt{2}y}{w_1} \right) \exp \left\{ - \left[i \frac{k}{2R_1} + \frac{1}{w_1^2} \right] (x^2 + y^2) \right\}. \quad (\text{A4})$$

A similar expression can be constructed for $u_{mn}(x, y, L_0)$ by replacing $w_1 \rightarrow w_2$ and $R_1 \rightarrow -R_2$ in Eq. (A4). We have not included the Gouy phase directly in these expressions; rather, we have chosen to treat the accumulation of the Gouy phase as a propagation effect. In other words, if we apply Eq. (5) to Eq. (A4) at $z' = z_1 = 0$, we obtain $-r_2 \exp(-i\varphi_{mn}/2) u_{mn}(x, y, L_0)$, where $-r_2$ is the amplitude reflectivity of mirror \mathcal{M}_2 , and

$$\varphi_{mn} \equiv 2(m + n + 1) \cos^{-1} \sqrt{g_1 g_2} \quad (\text{A5})$$

is the round-trip Gouy phase. Here the sign of the square root is chosen to be the same as the signs of g_1 and g_2 , which are identical in a stable resonator.

The Gouy phase causes a transverse mode-dependent shift in the resonance frequencies of the FPI. The frequency corresponding to the TEM_{mnq} mode is

$$\nu_{mnq} = \frac{c}{2L} \left[q + \frac{(m+n+1)\varphi_{00}}{2\pi} \right] \equiv q \Delta\nu_L + (m+n+1) \Delta\nu_G, \quad (\text{A6})$$

where $\Delta\nu_L \equiv c/2L$ is the free spectral range, and $\Delta\nu_G \equiv \Delta\nu_L \cos^{-1}(\sqrt{g_1 g_2})/\pi$ is the Gouy frequency shift.

For the LIGO FPI, we have $A = D = 1$, $B = L_0 = 3.99901$ km, and $C = 0$, resulting in the operating characteristics listed in table I. The stability factor for this configuration is $g_1 g_2 = 0.333$. The free spectral range is $\Delta\nu_L = 37.5$ kHz, corresponding to a round-trip time of $26.7 \mu\text{s}$, and the Gouy frequency shift is $\Delta\nu_G = 11.4$ kHz. Since the finesse of the FPI is approximately 200, the resolution of a fringe is only 185 Hz, which is far too small to permit an accidental coincidence of resonance frequencies for any low-order transverse modes.

When the FPI mirror apertures are finite, the above analysis may no longer apply. In particular, diffraction losses around the mirror apertures generally prevent the use of Eq. (A4) to describe the transverse spatial dependence of the field, which also result in a Gouy phase that no longer has the simple functional form of Eq. (A5). As an indicator of the magnitude of this problem for the LIGO FPI, we can compute the diffraction losses of a collection of low-order Hermite-Gauss modes at each of the FPI mirrors. We define the quantity

$$\begin{aligned} |\tilde{\gamma}_{jmn}|^2 &\equiv \int_{\mathcal{A}_j} dx dy |u_{mn}(x, y, z_j)|^2 \\ &= \frac{1}{2^{m+n} m! n! \pi} \int_0^{\zeta_j} d\rho \rho \exp(-\rho^2) \int_0^{2\pi} d\phi H_m^2(\rho \cos \phi) H_n^2(\rho \sin \phi), \end{aligned} \quad (\text{A7})$$

where $\zeta_j \equiv \sqrt{2}a/w_j$. Therefore, we can compute the diffraction loss $1 - |\tilde{\gamma}_{jmn}|^2$ as a function of ζ_j analytically using Mathematica, and then substitute the numerical values $\zeta_1 = 4.67$ and $\zeta_2 = 3.72$ for \mathcal{M}_1 and \mathcal{M}_2 , respectively. We find that the diffraction losses suffered upon reflection from \mathcal{M}_1 are substantially smaller than those obtained from \mathcal{M}_2 , but that these losses are larger than 1% for \mathcal{M}_2 when $m+n > 4$. Hence, we should restrict our analysis to Hermite-Gauss mode sets with $m+n \leq 4$.

* Also at Hewlett-Packard Laboratories, 13837 175th Pl. NE, Redmond, WA 98052-2180.

- [1] A. Abramovici, W. Althouse, J. Camp, J. A. Giaime, A. Gillespie, S. Kawamura, A. Kuhnert, T. Lyons, F. J. Raab, R. L. Savage Jr., D. Shoemaker, L. Sievers, R. Spero, R. Vogt, R. Weiss, S. Whitcomb, and M. Zucker, *Phys. Lett.* **A218**, 157-163 (1996).
- [2] A. Giazotto, in *First Edoardo Amaldi conference on gravitational wave experiments*, E. Coccia, G. Pizella and F. Ronga (eds.), (World Scientific, Singapore, 1995).
- [3] K. Danzmann, *ibid.*, 100.
- [4] K. Tsubono, *ibid.*, 112.
- [5] J.-Y. Vinet, B. J. Meers, C. N. Man, and A. Brillet, "Optimization of long-baseline optical interferometers for gravitational-wave detection," *Phys. Rev.* **D38**, 433-447 (1988).
- [6] M. W. Regehr, F. J. Raab, and S. E. Whitcomb, "Demonstration of a power-recycled Michelson interferometer with Fabry-Perot arms by frontal modulation," *Opt. Lett.* **20**, 1507-1509 (1995).
- [7] J.-Y. Vinet, P. Helló, C. N. Man, and A. Brillet, "A highly accuracy method for the simulation of non-ideal optical cavities," *J. Phys. I (Paris)* **2**, 1287-1303 (1992).
- [8] P. Saha, "Fast estimation of transverse fields in high-finesse optical cavities," *J. Opt. Soc. Am.* **A14**, 2195-2202 (1997).
- [9] B. Bochner, "Modelling the performance of interferometric gravitational-wave detectors with realistically imperfect optics," Ph. D. thesis, Massachusetts Institute of Technology, Cambridge (1998).
- [10] D. Z. Anderson, "Alignment of resonant optical cavities," *Appl. Opt.* **23**, 2944-2949 (1984).
- [11] E. Morrison, B. J. Meers, D. I. Robertson, and H. Ward, "Automatic alignment of optical interferometers," *Appl. Opt.* **33**, 5041-5049 (1994).
- [12] Y. Hefetz, N. Mavalvala, and D. Sigg, "Principles of calculating alignment signals in complex resonant optical interferometers," *J. Opt. Soc. Am.* **B107**, 1597-1605 (1997).
- [13] D. Redding, M. Regehr, and L. Sievers, "Dynamic models of Fabry-Perot interferometers," submitted to *Appl. Opt.*, 1998.
- [14] K. E. Oughstun, in *Progress in Optics*, Vol. **24**, E. Wolf, ed. (North-Holland, Amsterdam, 1987), pp. 165-387.
- [15] A. E. Siegman, *Lasers* (University Science Books, Mill Valley, 1986).
- [16] A. Gerrard and J. M. Burch, *Introduction to Matrix Methods in Optics* (John Wiley & Sons, New York, 1975).
- [17] P. M. Morse and H. Feshbach, *Methods of Theoretical Physics* (McGraw-Hill Book Co., New York, 1953), p. 904.

- [18] K. An, C. Yang, R. R. Dasari, and M. S. Feld, "Cavity ring-down technique and its application to the measurement of ultraslow velocities," *Opt. Lett.* **20**, 1068-1070 (1995).
- [19] M. J. Lawrence, B. Willke, M. E. Husman, E. K. Gustafson, and R. L. Byer, "The Dynamic Response of a Fabry-Perot Interferometer," submitted to *J. Opt. Soc. B*, 1999.
- [20] W. H. Press, S. A. Teukolsky, W. T. Vetterling, and B. P. Flannery, **Numerical Recipes in C: The Art of Scientific Computing** (Cambridge University Press, Cambridge, 1992).
- [21] L. Schnupp, Max Planck Institut für Quantenoptik, D-85748 Garching, Germany (personal communication, 1986).
- [22] R. G. Beausoleil, D. Sigg, and M. R. Zwickel, "Initial alignment tolerance of the LIGO interferometer," to be published.

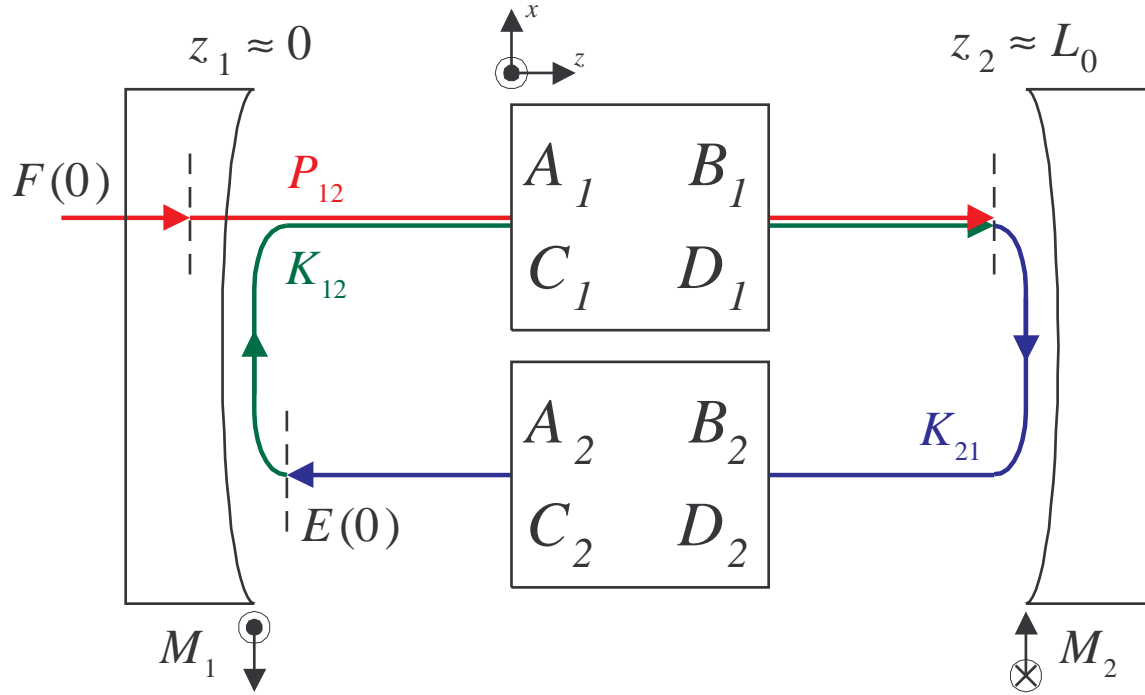


FIG. 1. Schematic of a generalized version of the LIGO two-aperture standing-wave resonator. The incident electric field amplitude function $F(\mathbf{r}, t)$ is transmitted through the (possibly misaligned) ITM and continues to propagate in the positive z direction. For LIGO, we have $A_2 = D_1$, $B_2 = B_1$, $C_2 = C_1$, and $D_2 = A_1$, with the specific values $A_1 = D_1 = 1$, $B_1 = L_0 \approx 4$ km, and $C_1 = 0$.

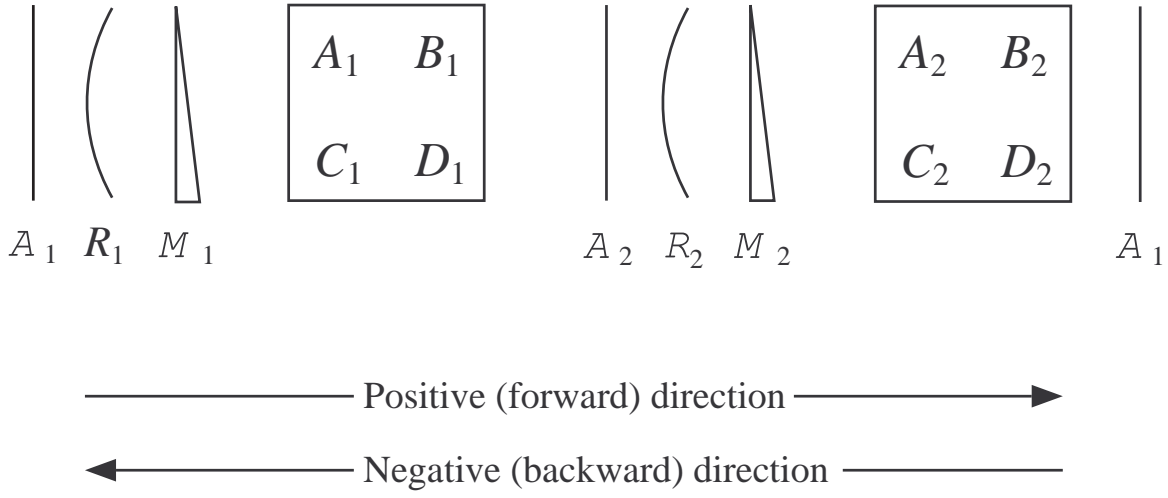


FIG. 2. The positive and negative propagation models corresponding to the resonator schematic shown in Fig. 1. \mathcal{A}_j , R_j , and \mathcal{M}_j respectively represent the aperture, radius of curvature, and anomalous phase distortion (caused by misalignment, for example) of either the ITM ($j = 1$) or the ETM ($j = 2$).

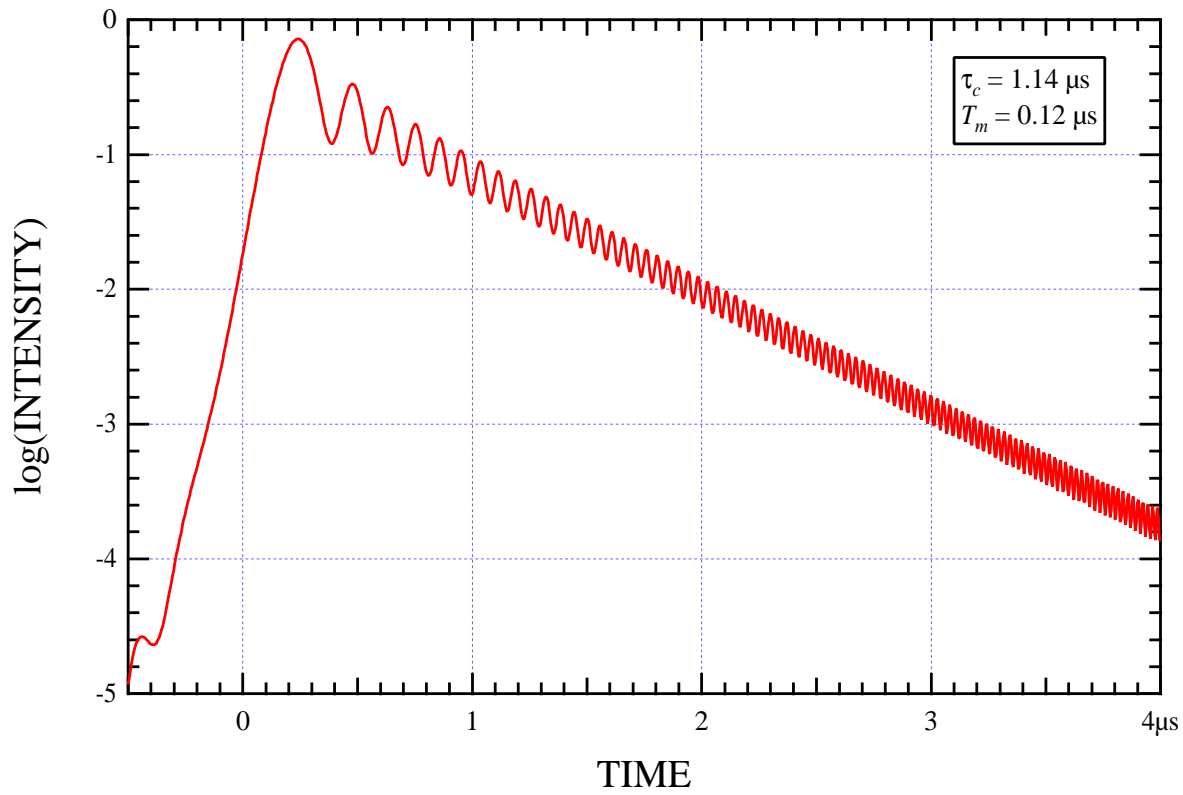


FIG. 3. Cavity decay curve computed by integrating Eq. (30) for the case where $\tau_c = 1.14\mu\text{s}$ and $T_m = 0.12\mu\text{s}$.

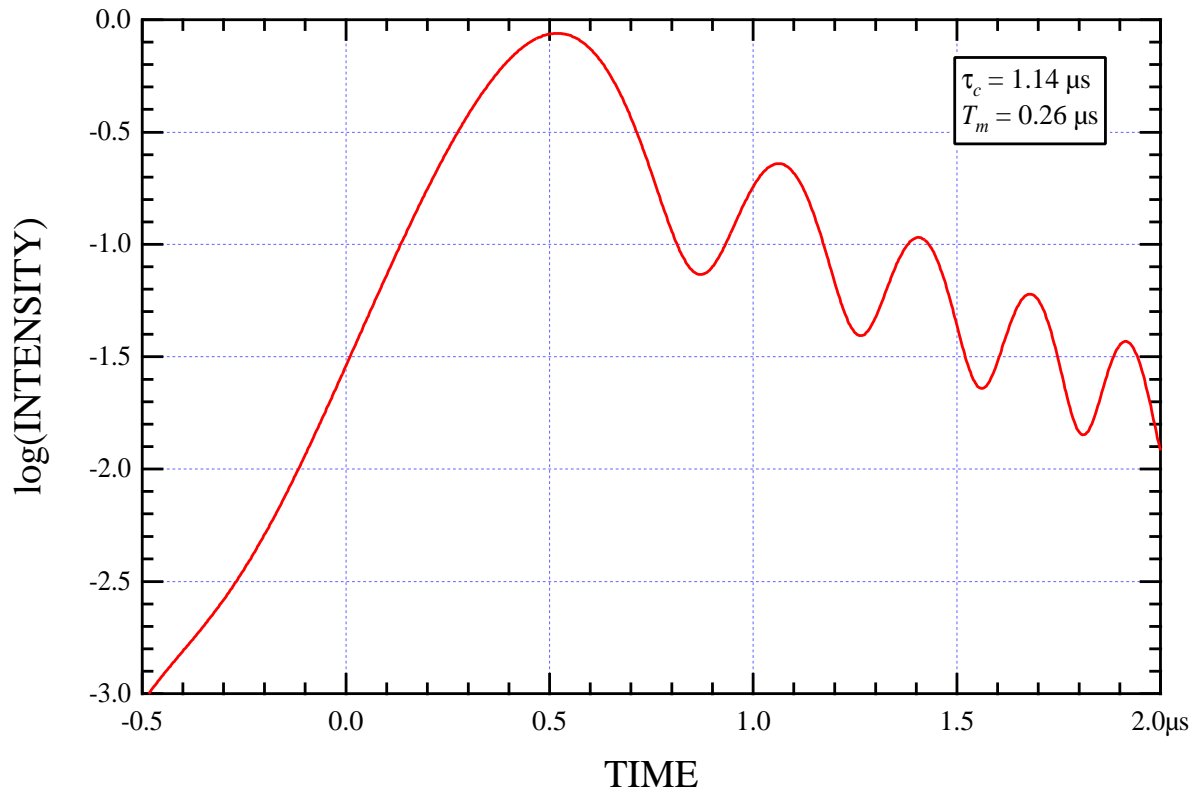


FIG. 4. Cavity decay curve computed by integrating Eq. (30) for the case where $\tau_c = 1.14\mu\text{s}$ and $T_m = 0.26\mu\text{s}$.

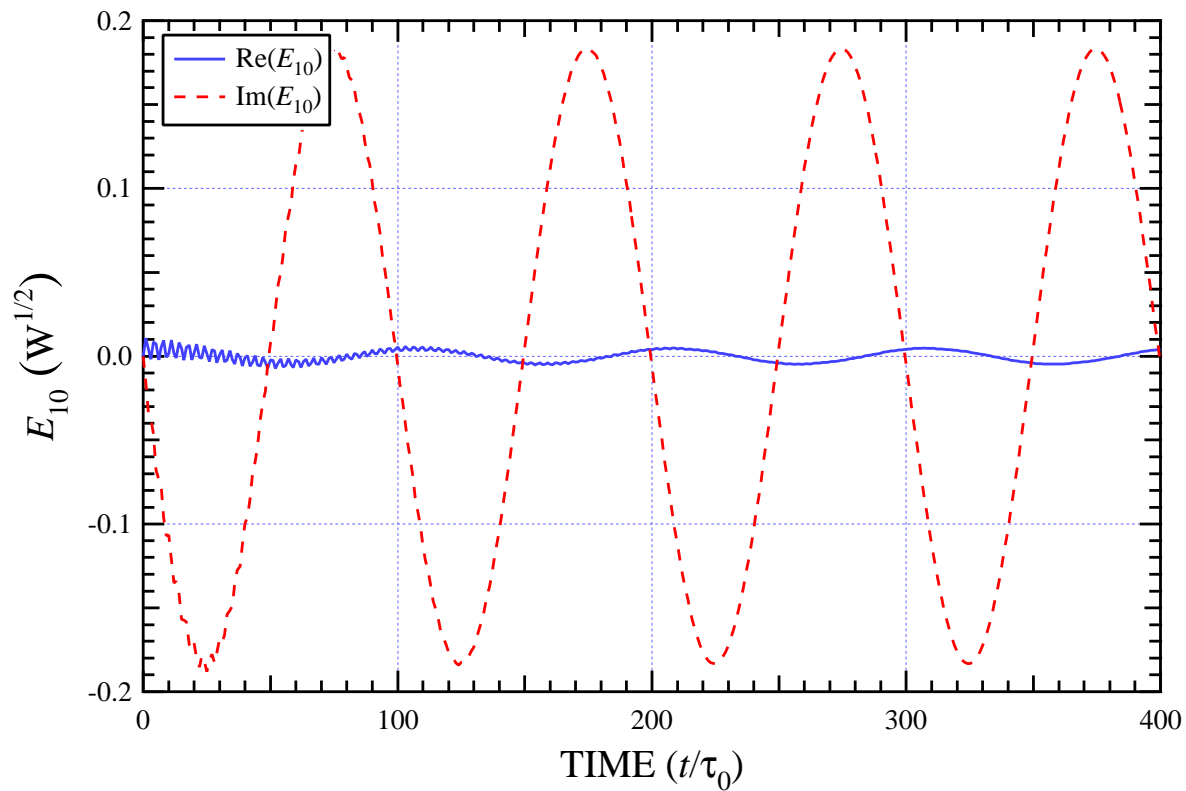


FIG. 5. Time evolution of the TEM_{10} component of the stored intracavity field at the optical carrier frequency as \mathcal{M}_2 is misaligned sinusoidally in the xz plane. The misalignment amplitude is $\Theta_m = 0.01$, and the oscillation period is $100\tau_0$. The input field is purely TEM_{00} , and has a power of 1 W.

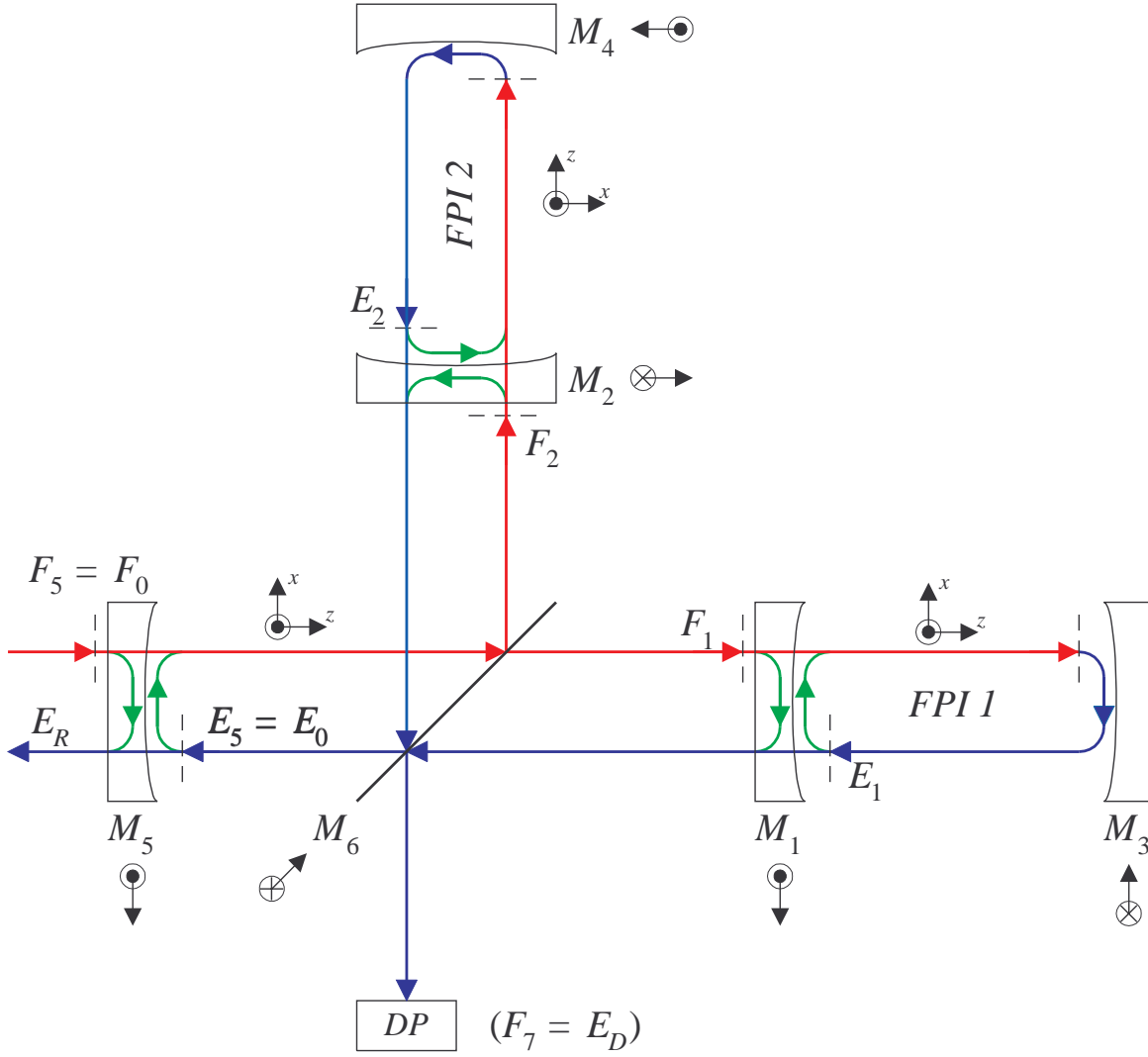


FIG. 6. Schematic of the primary optical components, electric fields, and conventions used in the LIGO IFO simulation. The coordinate systems for all fields propagating to the right or downward are right-handed, while those for propagation to the left or upward are left-handed. (The unit vector \hat{z} is always parallel with the direction of propagation, and \hat{y} is always directed towards the reader.) All angular rotation axes are defined so that a positive mirror misalignment causes the propagation vector — reflecting from the vacuum-coating interface of the mirror — to deflect away from the z axis in the positive direction.

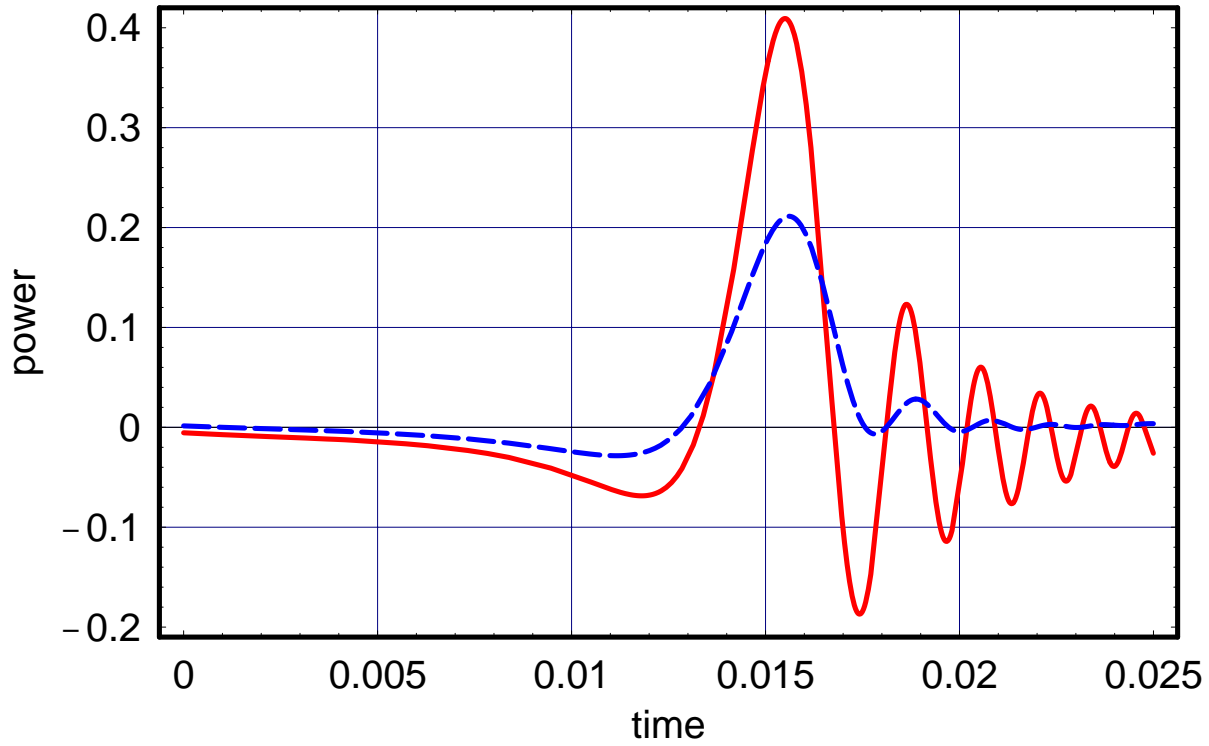


FIG. 7. Constant velocity scan of the in-line arm cavity rear mirror. Shown is the measured power of the demodulated quad-phase signal at the antisymmetric port using a monolithic photodetector. The solid curve shows the perfectly aligned case, whereas the dashed curve represents a misalignment of the scanning mirror of $2 \mu\text{rad}$. The scanning velocity is $1 \mu\text{m/s}$ over an interval of 0.025λ

TABLE I. Operating characteristics of the LIGO FPI.

Property	\mathcal{M}_1 (ITM)	\mathcal{M}_2 (ETM)
r^2 (reflectance)	0.96995	0.999935
t^2 (transmittance)	0.03	0.000015
R (radius of curvature)	14.571 km	7.400 km
a (aperture radius)	12 cm	12 cm
g (stability parameter)	$g_1 = 0.725$	$g_2 = 0.459$
w (RMS beam radius)	3.629 cm	4.57 cm
$\theta_{1/2}$ (beam expansion half-angle)	$9.65 \mu\text{r}$	$9.65 \mu\text{r}$

 TABLE II. Optical parameters of the components of the IFO power recycling cavity. The refractive index of all mirror substrates is 1.44968. The common-mode length of the recycling cavity is $l_C = 9.3800078186083$ m, the differential-mode distance is $l_D = 0.21$ m, and the distance between \mathcal{M}_5 and \mathcal{M}_6 is set as 4.38 m.

Property	\mathcal{M}_1 (ITM)	\mathcal{M}_5 (RM)	\mathcal{M}_6 (BS)
r^2 (reflectance)	0.96995	0.975	0.499625
t^2 (transmittance)	0.03	0.0244	0.499625
R (radius of curvature)	14.571 km	9.99833 km	∞
a (aperture radius)	12 cm	12 cm	12 cm
g (stability parameter)	$g_1 = 1.00093$	$g_5 = 0.999062$	NA
w (RMS beam radius)	3.629 cm	3.633 cm	3.631 cm
$\theta_{1/2}$ (expansion half-angle)	$9.65 \mu\text{r}$	$10.0 \mu\text{r}$	$10.0 \mu\text{r}$

TABLE III. Matrix operators required by the IFO power recycler connection equations in the adiabatic and Hermite-Gauss approximations, based on the conventions shown in Fig. 6.

Propagator	Coefficient	Phase	Operators
\hat{K}_{15}	$-ir_5t_6$	$\omega_q(\tau_C + \tau_D)/2 - 4\pi\Delta z_5$	$\hat{G}_{16}\hat{G}_{65}\hat{M}_5$
\hat{P}_{15}	$-t_5t_6$	$\omega_q(\tau_C + \tau_D)/2$	$\hat{G}_{16}\hat{G}_{65}$
\hat{K}_{51}	$-ir_1t_6$	$\omega_q(\tau_C + \tau_D)/2 + 4\pi\Delta z_1$	$\hat{G}_{56}\hat{G}_{61}\hat{M}_1^\dagger$
\hat{P}_{51}	$-t_1t_6$	$\omega_q(\tau_C + \tau_D)/2$	$\hat{G}_{56}\hat{G}_{61}$
\hat{K}_{25}	$-ir_5r_6$	$\omega_q(\tau_C - \tau_D)/2 - 4\pi(\Delta z_5 + \sqrt{2}\Delta z_6)$	$\hat{G}_{26}\hat{M}_6\hat{G}_{65}\hat{M}_5$
\hat{P}_{25}	$-t_5r_6$	$\omega_q(\tau_C - \tau_D)/2 - 4\sqrt{2}\pi\Delta z_6$	$\hat{G}_{26}\hat{M}_6\hat{G}_{65}$
\hat{K}_{52}	$-ir_2r_6$	$\omega_q(\tau_C - \tau_D)/2 + 4\pi(\Delta z_2 - \sqrt{2}\Delta z_6)$	$\hat{G}_{56}\hat{M}_6\hat{G}_{62}\hat{M}_2^\dagger$
\hat{P}_{52}	$-t_2r_6$	$\omega_q(\tau_C - \tau_D)/2 - 4\sqrt{2}\pi\Delta z_6$	$\hat{G}_{56}\hat{M}_6\hat{G}_{62}$
\hat{K}_{71}	ir_1r_6	$\omega_q(\tau_C + \tau_D)/2 + 4\pi(\Delta z_1 + \sqrt{2}\Delta z_6)$	$\hat{G}_{76}\hat{M}_6^\dagger\hat{G}_{61}\hat{M}_1^\dagger$
\hat{P}_{71}	t_1r_6	$\omega_q(\tau_C + \tau_D)/2 + 4\sqrt{2}\pi\Delta z_6$	$\hat{G}_{76}\hat{M}_6^\dagger\hat{G}_{61}$
\hat{K}_{72}	$-ir_2t_6$	$\omega_q(\tau_C - \tau_D)/2 + 4\pi\Delta z_2$	$\hat{G}_{76}\hat{G}_{62}\hat{M}_2^\dagger$
\hat{P}_{72}	$-t_2t_6$	$\omega_q(\tau_C - \tau_D)/2$	$\hat{G}_{76}\hat{G}_{62}$